# Modeling the Low-Frequency Sea Surface Temperature Variability in the North Pacific

UTE LUKSCH AND HANS VON STORCH

*Max-Planck-Institut für Meteorologie, Hamburg, Federal Republic of Germany*

(Manuscript received 19 April 1991, in final form 30 September 1991)

ABSTRACT

The question of whether the large-scale low-frequency sea surface temperature (SST) variability in the North Pacific can be interpreted as a response to large-scale wind anomalies is studied by an ocean general circulation model coupled to an advective model for the air temperature. Forced with observed monthly mean winds, the model is successful in reproducing the main space and time characteristics of the large-scale low-frequency SST variability. In winter also the simulated and observed SSTs are highly correlated.

The dominant process in producing wintertime SST tendencies is the anomalous turbulent heat exchange with the atmosphere that is parameterized by the bulk aerodynamic formula and takes into account the simulated air temperature, the simulated SST, and the observed winds. The oceanic response to turbulent momentum fluxes is much smaller. The horizontal scale of the simulated air temperature is induced by advective transports with the observed winds and transferred to the ocean by anomalous turbulent latent and sensible heat fluxes. The ocean response is lagging the atmospheric forcing by about one month and persists over much longer time than the atmospheric anomalies, particularly in winter.

Part of the observed low-frequency SST variance can be explained by teleconnection. A wind field that is directly related to the tropical El Niño–Southern Oscillation (ENSO) phenomenon produces SST anomalies with an ENSO-related variance of more than 50% instead of 10% to 30% as observed.

## 1. Introduction

Low-frequency sea surface temperature (SST) variability in the North Pacific is characterized by large-scale patterns (Namias 1969; Weare et al. 1976; Davis 1976) that often persist for more than 5 months. The persistence is considerably greater in winter than in summer (Namias et al. 1988). Seemingly, highly persistent SST periods occur simultaneously with large-scale atmospheric anomaly patterns (Namias et al. 1988). Wallace and Gutzler (1981) and Barnston and Livezey (1987) identified a series of typical patterns in the Northern Hemisphere monthly mean atmospheric circulation in winter. Two of them, in regions named Pacific–North America (PNA) and West Pacific Oscillation (WPO), are located in the North Pacific region. So, these large-scale atmospheric circulation patterns should be connected to the large-scale SST anomalies, but this relationship raises the question of cause and effect.

Large-scale air–sea interaction may be important for the variability of both ocean and atmosphere on monthly and seasonal time scales. Statistical analyses (Davis 1976; Wallace and Jiang 1987) of multiyear time series indicate that, at least in winter, the atmosphere is leading the ocean by about one month. Moreover, the horizontal scale of low-frequency SST variability is much greater than the oceanic Rossby deformation radius; it is, instead, similar to the scale of atmospheric circulation anomalies (Davis 1976; Namias and Cayan 1981; Wallace et al. 1990). These facts support the idea that a large part of the extratropical month-to-month SST variability may be explained by large-scale atmospheric forcing. On the other hand, the atmosphere is responding to the extratropical SST anomalies, too (Lau and Nath 1990; Alexander 1990). For a review of air–sea interaction in middle latitudes, the reader is referred to Frankignoul (1985).

The idea of the atmosphere being dominant in extratropical wintertime air–sea interaction on the month-to-month time scale was proposed first by Bjerknes (1962) for the North Atlantic. He argued that the mean atmospheric flow is responsible for the appearance of SST anomalies. An intensification of cold-air advection from the cold American continent would cool the warm Atlantic Ocean surface by an extra loss of heat due to anomalous latent and sensible heat fluxes and by a more efficient mixing of the upper level of the ocean. Likewise, a reduction in cold-air advection that normally prevails would be associated with a warming of the ocean surface. Zorita et al. (1992) derived the patterns of simultaneously occurring atmospheric flow and SST anomalies and found these patterns fully consistent with Bjerknes' hypothesis.

In the past, several model studies have been done to understand the ocean–atmosphere interaction in

*Corresponding author address:* Dr. Ute Luksch, Max-Planck-Institut für Meteorologie, Bundesstrasse 55, W-2000 Hamburg 13, Federal Republic of Germany.

midlatitudes (a good overview is given by Frankignoul 1985). Multilevel ocean circulation models were used by Haney et al. (1978), Huang (1979), and Haney (1980, 1985). They found that anomalous turbulent sensible and latent heating made a significant contribution to the development of the generated SST anomalies. They also found that wind anomalies alone generated SST anomalies that were correlated with the observed SST, but these anomalies are considerably too small (Haney et al. 1978; Haney 1985). The inclusion of observed anomalous surface heat fluxes derived from observations improved the simulations considerably. All of these studies used heat flux data that were derived from observed SST and air temperature data, and the air temperature is strongly coupled SST. So conclusions about the cause and effect are difficult to draw from these experiments. In the experiments described in this paper no information about the observed anomalous thermal structure in the ocean–atmosphere system is used. Instead, together with an advective model for the air temperature the observed wind forcing is used to simulate air temperature anomalies. This simulated air temperature is used (together with the simulated SST and the observed winds) to parameterize the wind-induced heat flux anomalies.

The global wind field is influenced by the tropical El Niño–Southern Oscillation (ENSO) phenomenon, as is the SST. About 10% to 30% of the low-frequency wintertime SST variance in the North Pacific can be attributed to atmospheric teleconnections excited by ENSO (Wright et al. 1985). Bjerknes (1969, 1972) already mentioned that ENSO influences the global atmospheric circulation and other investigations support his ideas (Horel and Wallace 1981; Wright et al. 1985; Mo and Livezey 1986; Livezey and Mo 1987; Hamilton 1988). The North Pacific SST is responding to the tropical phenomenon with a time lag of up to one month (Wright 1983; Wright et al. 1985). This fast connection between tropical and extratropical SST cannot be explained by oceanic processes alone (White et al. 1985). It lends support to the other famous hypothesis of Bjerknes (1969, 1972); namely, that atmospheric teleconnections are excited by tropical SST anomalies. To understand the processes involved in the tropical–extratropical SST interaction and what role the anomalous atmospheric circulation is playing in this connection, a experiment is carried out with ENSO-related wind anomalies.

In the present paper, a full oceanic general circulation model is used to investigate the low-frequency SST variability in the North Pacific. The ocean GCM and the advective model of the air temperature (AMAT) are presented in section 2. The results of a 30-year simulation, utilizing observed monthly mean winds from 1950 to 1979, are reported in section 3. In order to identify the physical processes that are dominant in the generation of SST anomalies, a number of sensitivity experiments were carried out (sections 4 and 5). Finally, in section 6, the influence of the tropical ENSO anomalies on the North Pacific SST by means of atmospheric teleconnections is discussed in terms of experiments with synthetic wind fields. In section 7 the results of the paper are summarized.

## 2. The model

The model we used in our experiments consists of an ocean GCM (OGCM) developed by Maier-Reimer (Max-Planck-Institut für Meteorologie, Hamburg) and an advective model of the air temperature (AMAT) to parameterize the influence of wind anomalies on the turbulent latent and sensible heat fluxes.

### *a. The ocean GCM*

The OGCM is based on the conservation of momentum, heat, salt, and volume simplified by the hydrostatic and Boussinesq approximations. The density of seawater is given by the equation of state (UNESCO 1981). At the surface the kinematic boundary condition is used. The horizontal turbulent eddy transport coefficients are set at constant values (turbulent viscosity: $2 \cdot 10^5$ m$^2$ s$^{-1}$; turbulent diffusivity: $D^H = 5 \cdot 10^2$ m$^2$ s$^{-1}$). The vertical mixing of momentum depends on the vertical shear of the ocean velocities and on the stratification, similar to the procedure in Pacanowski and Philander (1981). The vertical diffusivity coefficient $D^V$ is parameterized by the stratification only. The turbulent mixing of heat and salinity due to free convection is parameterized by convective adjustment.

The model is in spherical coordinates with a horizontal resolution of 3° × 3°. It has 13 layers in the vertical with highest resolution in the upper 200 m; a realistic topography is used. The analysis domain is the North Pacific from 28°N to 60°N. To avoid boundary problems the model domain was extended southward to 30°S. The near-surface ocean transports from the Southern Hemisphere in the analysis domain are small.

The ocean model was spun up for 50 years under climatological conditions including the whole seasonal cycle. For example, the momentum fluxes are given by the climatological wind stress from Hellerman and Rosenstein (1983) and, using the Newtonian formulation, temperature and salinity fields are coupled to observations. The climatological distribution of SST is from Comprehensive Ocean–Atmosphere Data Set (COADS) (monthly mean values; Woodruff et al. 1987). For the freshwater fluxes the yearly mean surface salinity from Levitus (1982) is used because of the lag of better seasonal information. The observed mean state in the upper ocean of the analysis domain, that is, from 28°N to 60°N, is reproduced satisfactorily by the model (Luksch et al. 1990).

After the spinup Newtonian cooling is no longer used

because this parameterization strongly damps SST anomalies in the ocean model. Instead of this, the climatological heat flux $\tilde{Q}$ was derived as the flux that is necessary for the ocean model to reproduce the observed climatological SST with a relaxation time of about 10 days. Thus,

$$\tilde{Q} = \rho c_p z \epsilon (T^C_{\text{obs}} - \tilde{T}); \qquad \epsilon = 1 \times 10^{-6} \quad (1/\epsilon \approx 10 \text{ days}). \quad (1)$$

Here, $\rho$ is the density of ocean water, $c_p$ the specific heat, and $z$ the thickness of the first ocean layer; $T^C_{\text{obs}}$ is the observed climatological SST, and $\tilde{T}$ the simulated ocean temperature of the first ocean layer at the end of the spinup. With this climatological heat flux the upper ocean is (cyclo-)stationary.

Large-scale atmospheric circulation anomalies can modify the momentum and heat fluxes at the ocean surface, thus creating ocean temperature tendencies. These effects are included in the prognostic equation for the ocean temperature:

$$T_t = \underbrace{-\mathbf{u}\nabla T - wT_z}_{\text{I}} + \underbrace{\nabla(D^H \nabla T) + (D^V T_z)_z}_{\text{II}} + \underbrace{\delta[Q^*_{HS} + Q^*_{HL} + \tilde{Q}]/(\rho c_p z)}_{\text{III}}, \quad (2)$$

where $T$ is the ocean temperature, $\mathbf{u}$ the horizontal ocean velocity vector, and $w$ the vertical velocity. Here $Q^*_{HS}$, $Q^*_{HL}$ are the anomalous turbulent sensible and latent heat flux anomalies at the ocean surface, and $\tilde{Q}$ is the climatological heat flux for the ocean model (surface: $\delta = 1$; otherwise: $\delta = 0$). Positive heat fluxes result in a positive impact in the ocean. The index $t$ stands for time derivative, and the index $z$ for vertical derivative. The superscript $C$ stands for the mean over the simulation period (1950–1979), and * stands for its deviation.

In (2) there are various processes that depend on the imposed anomalous wind and induce SST tendencies:

I. advective transports in the ocean
II. heat transports due to turbulent mixing in the ocean
III. turbulent heat exchange between ocean and atmosphere.

The turbulent latent and sensible heat fluxes are parameterized by the simulated air temperature (AMAT), the simulated SST, and the observed wind data. The influence of an anomalous heat flux due to cloud-induced radiation changes is not considered here. The momentum fluxes used in the equation of motion are directly derived from the observed winds [Comprehensive Ocean–Atmosphere Data Set (COADS); Woodruff et al. 1987, section 3]. The heat flux parameters from COADS are not used for this study because these anomalies are computed from the actual observed air temperature and SST data.

### b. *The advective model of the air temperature*

According to Bjerknes' hypothesis for the North Atlantic (see section 1), we consider large-scale atmospheric circulation anomalies as the dominant factor in changing the extratropical wintertime air–sea interaction. Anomalous advective transports produce air temperature tendencies that modify the turbulent heat exchange between ocean and atmosphere. These air temperature tendencies shall be reproduced by the AMAT, and the simulated values are used for the bulk aerodynamic formula (see section 2c).

AMAT consists of one prognostic equation for the low-level air temperature $T^A$:

$$T^A_t = \underbrace{-\mathbf{u}^A \nabla T^A}_{\text{I}} + \underbrace{[-Q^*_{HS}}_{\text{III}} + \underbrace{Q_D}_{\text{II}} + \tilde{Q}]/(\rho^A c^A_p H^A); \quad (3)$$

$\rho^A$ is the density of the air, $c^A_p$ is its specific heat, and $H^A$ the height of the homogeneous atmosphere. Here $Q^*_{HS}$ is the anomalous sensible heat flux already present in (2) but here multiplied by $-1$ (heating the ocean means cooling the atmosphere and vice versa). Because of its rapid adjustment, AMAT was started from observed climatological conditions without a spinup. Over land the air temperature is fixed to the observed climatological values $T^{AC}_{\text{obs}}$.

Here $\tilde{Q}^A$ is the climatological heat flux for AMAT. As in (1) for the ocean model the climatological heat flux is determined before the experiments as the amount of energy needed for the model to reproduce the observed climatological air temperature $T^{AC}_{\text{obs}}$ with a relaxation time of one time step:

$$Q^A = \rho^A c^A_p H^A \epsilon^A (T^{AC}_{\text{obs}} - \tilde{T}^A); \quad 1/\epsilon^A = 4 \text{ h}; \quad (4a)$$

$\tilde{T}^A$ is the simulated air temperature under climatological wind conditions.

The damping term $Q_D$ is included to parameterize those unresolved processes, such as baroclinic processes, turbulence, and cloud/radiation processes, which are capable of destroying air temperature anomalies:

$$Q_D = \rho^A c^A_p H^A \epsilon_D (T^{AC}_{\text{obs}} - T^A) \quad (4b)$$

with $\epsilon_D = (5 \text{ days})^{-1}$ in the analysis domain (28°N to 60°N). Outside of this area the damping is stronger [$\epsilon_D = (1 \text{ days})^{-1}$], because only the local forcing by the extratropical atmosphere shall be considered here. Note that no information about the observed anomalous temperature values is used.

Three nonconstant processes are taken into account in (3), namely:

I. advection by the observed monthly mean wind $\mathbf{u}^A$

II. the anomalous sensible heat flux $Q^*_{HS}$ representing the ocean–atmosphere interaction

III. a damping term $Q_D$.

The anomalous latent heat flux $Q^*_{HL}$ is not considered in AMAT because the region where condensation takes place is not known. A sensitivity experiment is carried out to estimate the influence of $Q^*_{HL}$ on the air temperature (section 5: experiment A3).

The height of the model layer $H^A$ is chosen according to the height of the atmospheric response to anomalous SST in an AGCM (Chervin et al. 1980). The air temperature response to the diffusion term $Q_D$ and to the climatological heat flux $Q^{AC}$ is independent of $H^A$ [see (3) and (4a,b)]. On the other hand, a decrease of $H^A$ leads to an increase of the SST forcing [term II in (3)]. For example, halving $H^A$ doubles the impact of $Q^*_{HS}$ on the SST. In winter, latent and sensible heat flux anomalies are positively correlated (Cayan 1990), so the oceanic impact should be similar for a decrease of $H^A$ and the inclusion of latent heat flux forcing done in experiment A3.

### c. *The anomalous heat fluxes*

The anomalous sensible and latent heat fluxes, $Q^*_{HS}$ and $Q^*_{HL}$, are derived by subtracting the climatological sensible and latent heat fluxes, $Q^C_{HS}$ and $Q^C_{HL}$, from the simulated values; that is,

$$Q^*_{HS} = Q_{HS} - Q^C_{HS} \quad \text{and} \quad Q^*_{HL} = Q_{HL} - Q^C_{HL}.$$

The actual heat fluxes are derived from the conventional bulk formula (e.g., Neumann and Pierson 1966):

$$Q_{HS} = \rho^A c_p^A c_H \cdot |\mathbf{u}^A| \cdot (T^A - T)$$

$$\text{and} \quad Q_{HL} = -\rho^A L c_E \cdot |\mathbf{u}^A| \cdot (s^s - s) \quad (5)$$

with $c_H = c_E = 1.3 \times 10^{-3}$ (Hasse and Dobsen 1986); $s$ is the specific humidity of the air derived from the observed climatological relative humidity and the simulated air temperature. Here $s^s$ is the specific humidity assuming 100% relative humidity and an air temperature equal to the ocean temperature at the surface.

The climatological values $Q^C_{HS}$ and $Q^C_{HL}$ are derived from the climatological temperature, humidity, and wind data.

## 3. The basic experiment

In the basic experiment the model (AMAT and OGCM) is forced by observed monthly mean wind fields, $\mathbf{u}^A$, the derived momentum fluxes (COADS; Woodruff et al. 1987) for the period 1950–1979, and by simulated heat fluxes ($Q^*_{HL}$, $Q^*_{HS}$). The observed monthly mean wind anomalies are averaged onto 10° × 4° longitude/latitude boxes. Thus, high-frequency and small-scale processes are not included in the forcing. The schematic of this experiment is

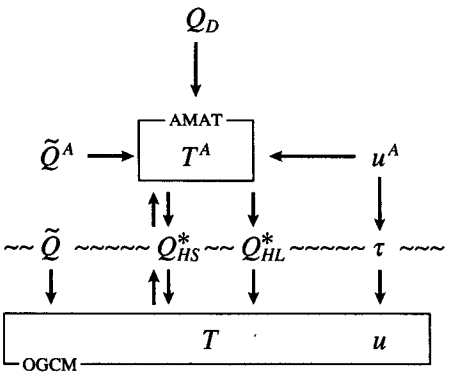


BASIC EXPERIMENT.

For this experiment no information about the anomalous observed thermal structure in atmosphere and ocean is used. The anomalous heat fluxes ($Q^*_{HL}$, $Q^*_{HS}$) are parameterized by the simulated temperatures $T$ and $T^A$ and the observed wind data. Heat flux anomalies from COADS are computed by the observed anomalous air temperature and SST data and shall not be used here.

In the following, a statistical discussion of the observed and simulated SST anomalies for the period 1950–1979 in the analysis domain (28°N to 60°N) is given. For that the data are averaged over a month (360 months). To derive the dominant low-frequency EOFs the data are bandpass filtered. The unfiltered data are projected on these derived EOFs. For the other statistics unfiltered data are used.

### a. *EOF analysis*

The first EOF of the observed SST describes 23% of the total variance. A negative SST anomaly in the central North Pacific (near 40°N and the date line) is connected with a positive anomaly near the North American coast, and vice versa (Fig. 1a). The distance between the centers of negative and positive SST anomaly is about 4000–6000 km. This is much larger than the oceanic Rossby deformation radius (Wallace et al. 1990) and, instead, comparable to the characteristic scale of the atmospheric circulation. In the simulation the horizontal scale of the SST pattern is reproduced, and the first EOF describes 24% of the total variance (Fig. 1b). The center of the coastal anomaly is shifted to the southwest. The second EOFs describe 19% of the total variance in the observation and 20% in the simulation. They are large scale, too, with a strong anomaly near 40°N and 160°W and a weaker anticorrelated anomaly near the North American coast (Fig. 2).

The lifetime of the anomalies is defined by the autocorrelation coefficients of the EOF time series. In the observations the first EOF persists in winter for 4 to 6 months and in summer for a much shorter time (Fig.

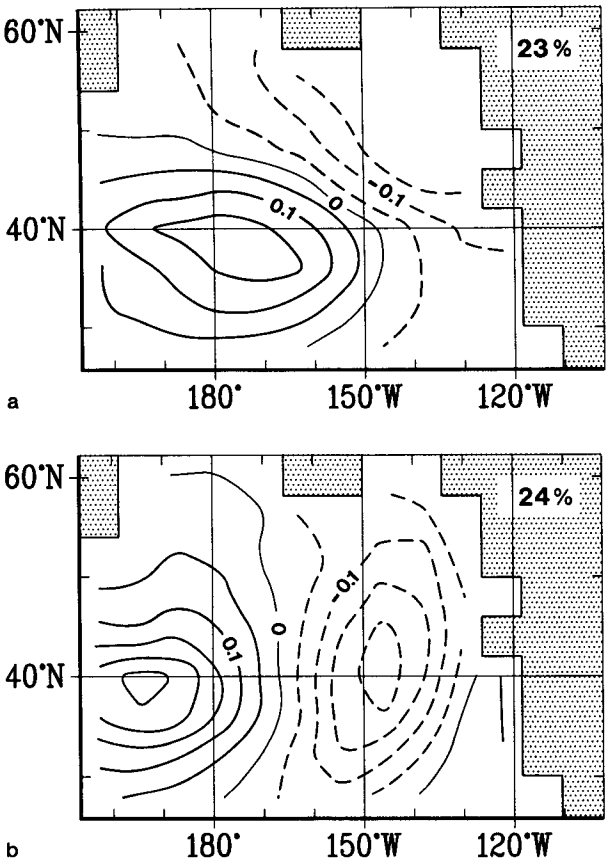


FIG. 1. First EOF of observed and simulated SST anomalies (1950–1979; 360 months; bandpass filter: 3–30 months; time coefficients: Fig. 3; units: K). (a) Observations (COADS), explained variance: 23%. (b) Simulation (basic experiment), explained variance: 24%.

3a). The second pattern exhibits this seasonal cycle, too, with a shorter lifetime during summer and a longer lifetime in winter (not shown). The time scales of oceanic (SST) and atmospheric variables (wind, air temperature) are very different. The persistence of wind anomalies is considerably shorter than the persistence of the oceanic variables and without a pronounced seasonal cycle (cf. Fig. 3 and Fig. 4). This supports the results of the stochastic climate models that explain the red response spectrum of the SST as an integrated response to the white spectrum of the atmospheric forcing (section 1). The oceanic seasonal cycle of persistence of the large-scale pattern is reproduced by the model as a response to the observed large-scale wind anomalies, as can be seen in the autocorrelations for the first EOF shown in Fig. 3b. The wintertime correlation coefficient between observed and simulated EOF time series is about 0.55 for the first EOF and 0.65 for the second EOF, implying that the relatively persistent winter patterns can be reproduced by the model. In summer, however, the time series are uncorrelated.

### *b. Local analysis*

The observed wintertime variability of monthly mean SST is high, near 40°N in the zone of strong westerly winds (Fig. 5a). This is well reproduced in the model (Fig. 5b; unfiltered data). In this area of high SST variability the local wintertime correlation coefficients, derived from 30 statistically independent pairs of simulated and observed January SSTs, are greater than 0.5 (Fig. 6a). With the assumption that the temperature is Gaussian distributed, a correlation coefficient of 0.54 is significantly nonzero at the 99.9% level. In summer (July) the correlation coefficients are much smaller (Fig. 6b).

The correlation coefficients decrease in spring (March, April) and increase in autumn (September, October). That means that the correlations are high when the persistence of the large-scale SST anomalies is also high (section 3a), the mixed layer is deep (100 to 200 m; Levitus 1982), and the latent and sensible heat flux anomalies outweigh those of the radiative

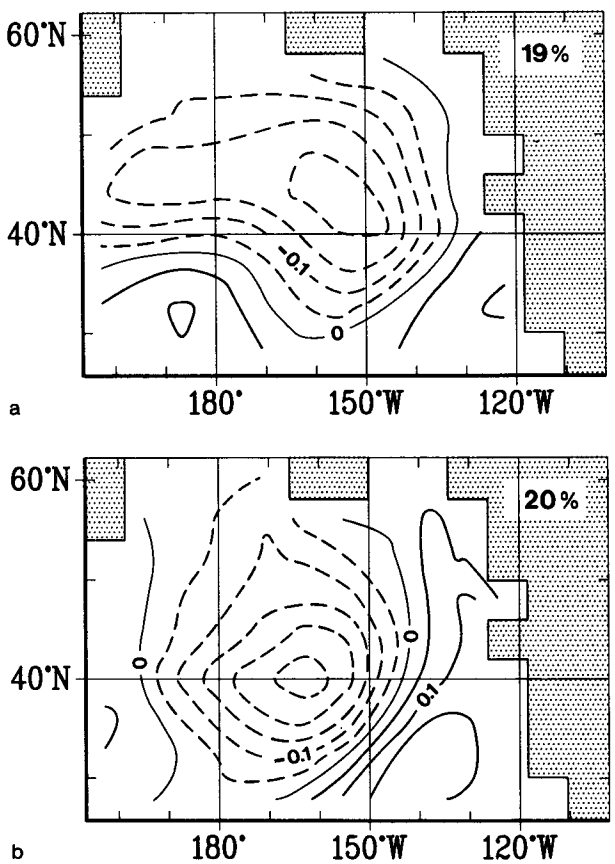


FIG. 2. Second EOF of observed and simulated SST anomalies (1950–1979; 360 months; bandpass filter: 3–30 months; time coefficients: Fig. 4; units: K). (a) Observations (COADS), explained variance: 19%. (b) Simulation (basic experiment), explained variance: 20%.

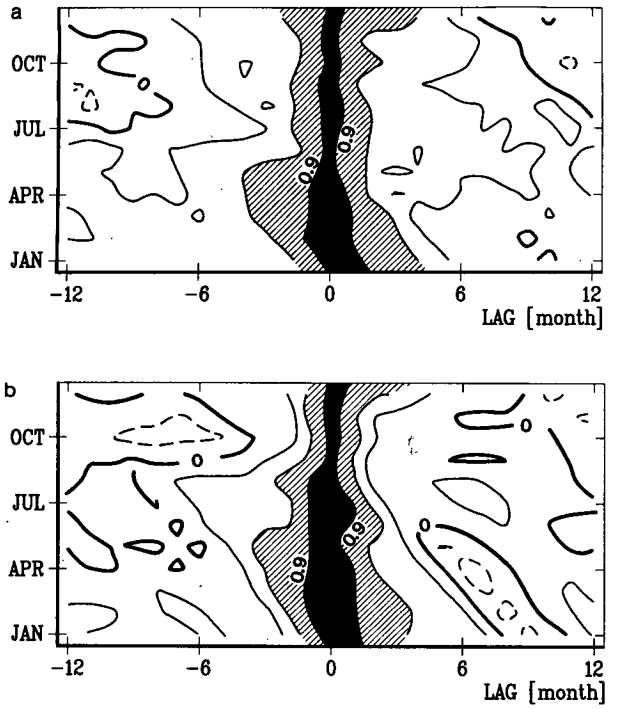


FIG. 3. Autocorrelation coefficients of the EOF time series (first EOF of simulated and observed SST anomalies; see Fig. 1) for different seasons (January to December) and different lags (−12 to zero to 12 months). Black area: values greater than 0.9; hatched area: 0.6 to 0.9; dashed lines: negative values. (a) Observation (COADS). (b) Simulation (basic experiment).

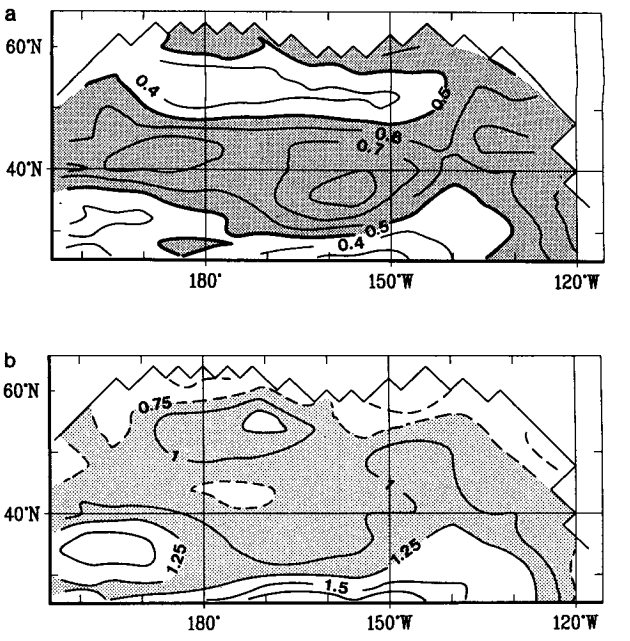


FIG. 5. Month-to-month variability of observed and simulated January SST. (a) Standard deviation of the observed SST anomalies (COADS, 1950–1979). Areas with standard deviations greater than 0.5°C are stippled. Contour interval 0.1 C. (b) Ratio of standard deviations of observed and simulated January SST (basic experiment). Ratios less than 1 indicate an underestimation by the model. Areas with ratios between 0.75 and 1.25 are stippled. Contour interval 0.25.

fluxes (Cayan 1990). The correlations are low when the lifetime of the SST anomalies is reduced, the mixed layer is very shallow (20 to 50 m), and the SST impact on shortwave radiation anomalies is stronger. High-frequency and small-scale processes like clouds and their impact on the radiation budget are not considered in the model. In spring synoptic winds may also be important for the development of the mixed layer (Frankignoul 1979), which is not included in the forcing, either. To get better summer results the forcing due to synoptic winds and clouds should be added and the vertical resolution of the ocean model should be enhanced or a mixed-layer model should be embedded in the ocean GCM. In winter the model is able to reproduce the persistent large-scale SST anomalies, and therefore, it is worthwhile to discuss the mechanisms acting in the model during this season.

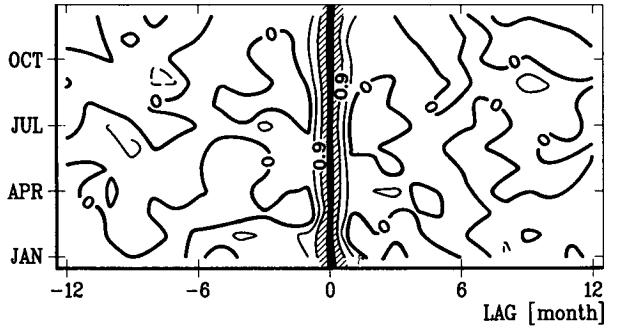


FIG. 4. Autocorrelation coefficients of the EOF time series (first EOF of the observed wind anomalies; see Fig. 8a) for different seasons (January to December) and different lags (−12 to zero to 12 months). Black area: values greater than 0.9; hatched area: 0.6 to 0.9; dashed lines: negative values.

### c. *Processes*

To find out which of the aforementioned processes (I–III) was dominant in the basic experiment during wintertime, the horizontal distribution of the standard deviation of the respective contributions in Eq. (2) was analyzed. The result of this diagnosis, for the winter months, is depicted in Fig. 7. The most important process is III, the turbulent heat fluxes, $Q^*_{HL}$ and $Q^*_{HS}$: it accounts for up to 60 to 70 W m$^{-2}$. The second most important process is I, the oceanic advection that is associated with a maxima of 25 W m$^{-2}$. This is mainly due to the horizontal transport mechanisms except in the far north near the coast where the vertical advection

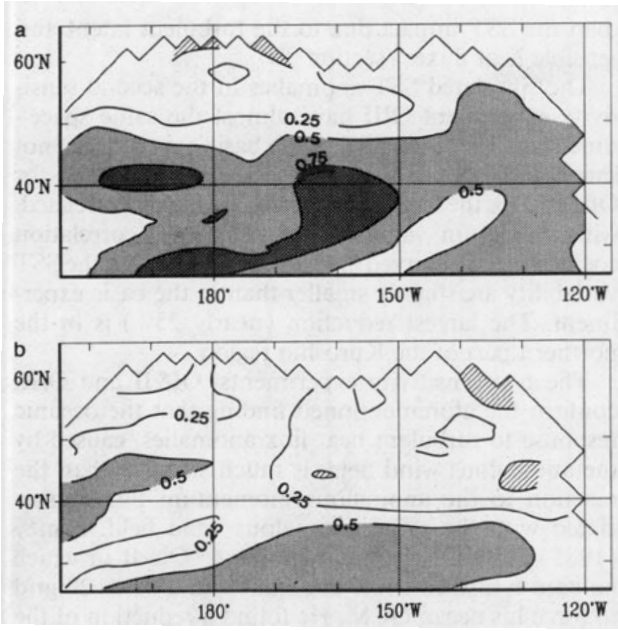


FIG. 6. Local correlation coefficients between observed (COADS) and simulated SST (basic experiment; 30 month; contour interval: 0.25). Areas with correlation coefficients greater than 0.50 (0.75) are stippled (dark stippled). Areas with negative values are hatched. (a) January, (b) July.

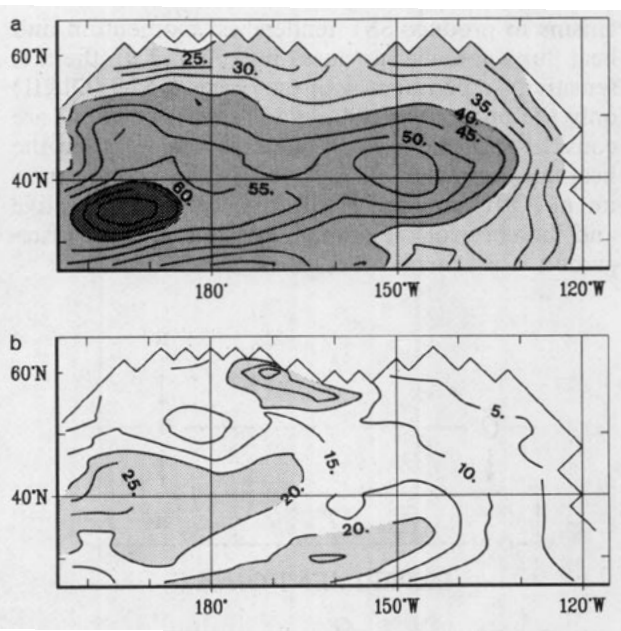


FIG. 7. Month-to-month variability of wind-induced SST tendencies in January (units: W $m^{-2}$; basic experiment). Areas with standard deviations greater than 20 (40/60) W $m^{-2}$ are light (middle/dark) stippled. Contour interval 5 W $m^{-2}$). (a) Standard deviation of the sum of turbulent latent and sensible heat flux anomalies. (b) Standard deviation of the heat flux anomalies due to anomalous advective transports in the ocean.

is dominating. The turbulent mixing in the ocean, process II, has a negligible effect ($\leq$5 W $m^{-2}$; not shown).

To find out how realistic the simulated turbulent heat flux anomalies are, a comparison with "observed" heat flux data was carried out. First, the simulated data were correlated with heat flux data computed by the observed monthly mean temperature and wind data and these fluxes are highly correlated (Fig. 8). The "observed" fluxes do not include the fluctuations of temperature and wind data smaller than one month. Therefore, we also compare the simulated heat fluxes with the COADS heat flux anomalies derived from actually observed temperature and wind data ($c_H = c_E = 1.3 \times 10^{-3}$). These data are very noisy. After smoothing these anomalies are also highly correlated with the simulated flux anomalies. The correlation pattern is very similar to Fig. 8, and the correlation coefficients are slightly reduced. The highest correlation coefficients are about 0.75. On most grid points of the analysis area the value is higher than 0.5.

The simulated air temperature is directly responding to wind-field anomalies, whereas the simulated SST is lagging the atmospheric forcing by about 1 month. The lagged cross-correlation functions look very similar to the cross correlation between time series of the dominant EOFs from observed SST and SLP anomalies (Davis 1976; see also Frankignoul 1985). The time scale of SST anomalies, for example, the strong seasonal cycle with a high persistence during wintertime, is different from atmospheric time scales and connected to the ocean dynamics. The horizontal scale of the SST anomalies is nearly identical to the horizontal scale of the simulated air temperature anomalies, which are mainly produced by anomalous advective transports with the observed wind field, as discussed later in section 5 and transfered to the ocean by turbulent latent and sensible heat fluxes.

## 4. Sensitivity experiments with the ocean model

Two sensitivity experiments are carried out, allowing us to discuss the relevance of the two different mech-

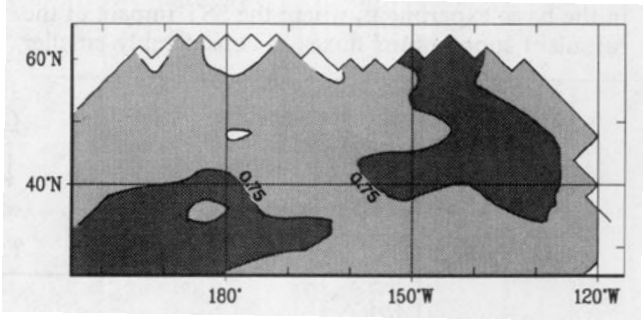


FIG. 8. Local correlation coefficients in January between heat flux anomalies derived from the observed temperatures (COADS) and simulated temperatures (basic experiment; 30 month; contour interval: 0.25). Areas with correlation coefficients greater than 0.50 (0.75) are stippled (dark stippled). Areas with negative values are hatched.

anisms to produce SST tendencies: momentum and heat flux anomalies as stated in section 2. In the first sensitivity experiment with the ocean model (OI&II) only the processes I (advection) and II (mixing) are considered in the temperature equation (2), and the heat flux anomalies are dropped. In the second experiment (OIII) only process III, the heat fluxes, is active and the effect of the anomalous wind stress is disregarded. The schematics for these experiments are

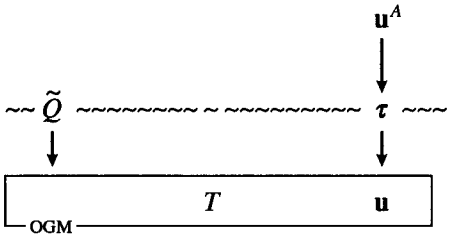


EXPERIMENT OI&II

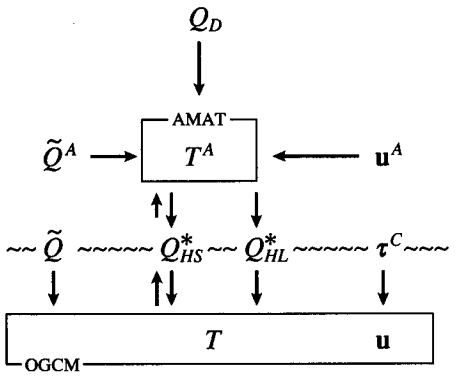


EXPERIMENT OIII ($\tau = 0$).

In experiment OI&II, the simulated SST variability is, in terms of its standard deviation, only one-third of the observed variability (not shown). Moreover, the persistence of the anomalies is much too high (Fig. 9). This result is consistent with the finding in section 3b in the basic experiment, where the SST impact of the turbulent momentum fluxes is considerably smaller than the SST impact due to the turbulent latent and sensible heat fluxes (section 3b).

The simulated SST anomalies in the second sensitivity experiment OIII have almost the same space–time statistics as the SST of the basic experiment (not shown). The EOF time series, derived separately for OIII and for the basic experiment, are highly correlated, with maximum values of 0.9. The local correlation coefficients of observed and simulated SST and the SST variability are slightly smaller than in the basic experiment. The largest reduction (nearly 25%) is in the northern part of the Kuroshio region.

The two sensitivity experiments, OI&II and OIII, confirm the aforementioned finding that the oceanic response to turbulent heat flux anomalies, caused by the anomalous wind field, is much stronger than the reaction to the anomalous momentum fluxes associated with the same anomalous wind field. Haney (1985) did an experiment similar to OI&II in which he used 6-h wind-stress anomalies on a 3° × 2° grid to force his ocean GCM. He found a reduction of the SST variability similar to what we found in experiment OI&II.

## 5. Sensitivity experiments with AMAT

In the previous section we found that the dominant process in generating North Pacific SST is the turbulent heat exchange between atmosphere and ocean. In our model environment, AMAT is dominant in modeling this process. Therefore, it is worth investigating the quality of AMAT and the relative importance of two explicitly described processes in AMAT, namely, the horizontal advection by the wind and the heat exchange with the ocean [see (3)]. For that purpose, three sensitivity experiments are conducted with AMAT. In experiment A1, AMAT is forced with 30 years of observed SST instead of the simulated SST as in section 4. By examining this experiment we can verify AMAT in the absence of ocean model deficiencies. In experiment A2 the turbulent heat exchange is disregarded, whereas in experiment A3 in addition to the anomalous sensible heat flux, turbulent latent heat flux anomalies have also been included. Schematically these experiments can be represented by

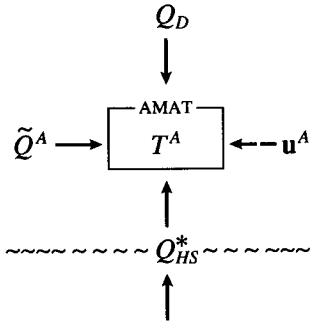


observed SST
EXPERIMENT A1

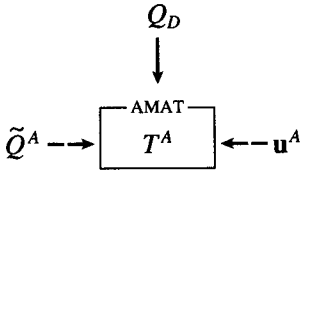


EXPERIMENT A2

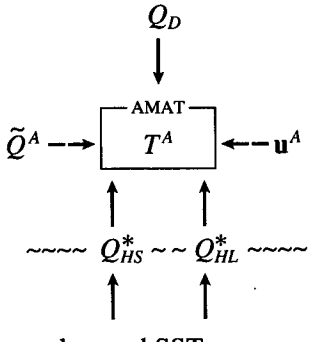


observed SST
EXPERIMENT A3.

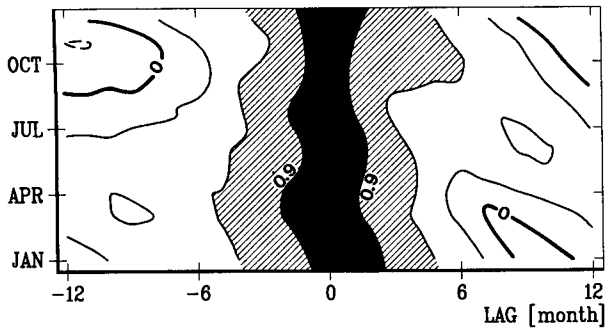


FIG. 9. Autocorrelation coefficients of the EOF time series (first EOF of the simulated SST anomalies; experiment OI&II: no heat flux anomalies) for different seasons (January to December) and different lags (−12 to zero to 12 months). Black area: values greater than 0.9; hatched area: 0.6 to 0.9; dashed lines: negative values.

The parameter simulated by AMAT is low-level air temperature. To evaluate the performance of AMAT, the simulated statistics of air temperature have to be compared with the statistics derived from the observations. Particular emphasis will be laid on the question of how the spatial scale and the time scale of air temperature anomalies are maintained by AMAT.

We have considered observed air temperature as revealed by COADS. The leading EOFs of this parameter, the first of which is shown in Fig. 10a, are, not unexpectedly, very similar to the observed SST anomalies (Fig. 1a). So the areas of high winter variability are similar for these two fields. The observed air temperature has a band of high variability near 40°N and near the west coast of North America, just as SST does (Fig. 5a and Fig. 11a). The high similarities of SST and air temperature are the reason that the heat flux anomalies from COADS (derived from the observed temperature, humidity, and wind anomalies) are not used to force the ocean GCM. The characteristic time scale of air temperature anomalies, as revealed by the seasonal autocorrelation function depicted in Fig. 12a, is considerably shorter than that of SST (Fig. 3) but comparable to that of the wind (Fig. 4). The lifetime of the large-scale air temperature anomalies is independent of the season and is smaller than 1 to 2 months. Therefore, the observed and simulated long wintertime persistence of the SST anomalies is caused by oceanic mechanisms and not by atmospheric processes, whereas the spatial scale is atmospheric in origin.

The leading EOFs of the simulated air temperature in experiment A1, where AMAT is forced with ob-

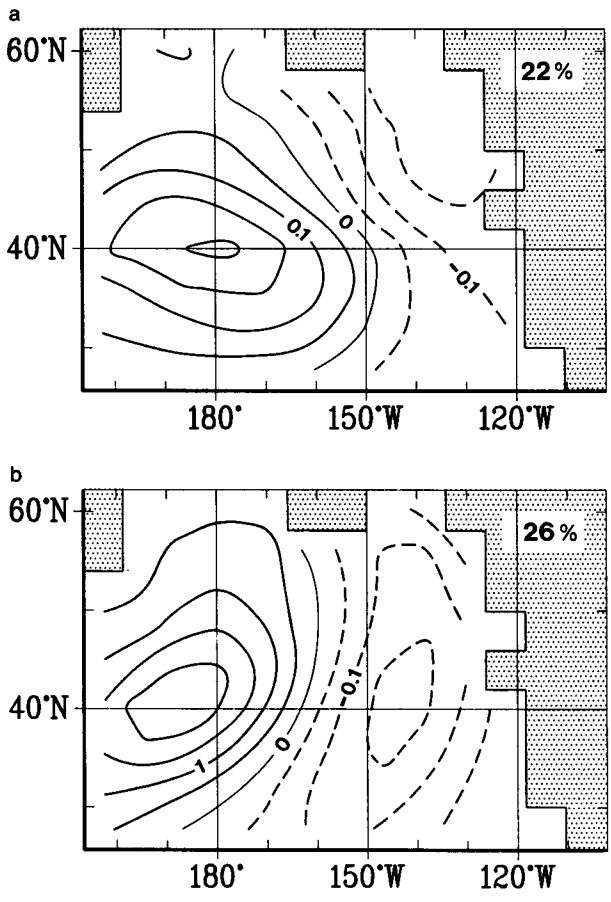


FIG. 10. First EOF observed and simulated air temperature anomalies (1950–1979; 360 months; bandpass filter: 3–30 months; units: K). (a) Observations (COADS), explained variance: 22%. (b) Simulation (experiment A1: uncoupled), explained variance: 26%.

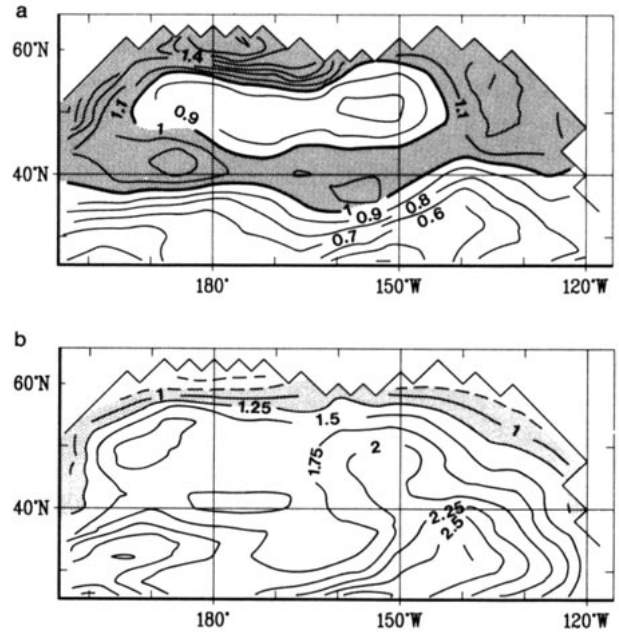


FIG. 11. Month-to-month variability of observed and simulated January air temperature. (a) Standard deviation of the observed air temperature anomalies (COADS, 1950–79). Areas with standard deviations greater than 1.0 K are stippled. Contour interval 0.1 K. (b) Ratio of standard deviations observed and simulated January air temperature (experiment A1: uncoupled). Ratios less than 1 indicate an underestimation by the model. Areas with ratios between 0.75 and 1.25 are stippled. Contour interval 0.25.

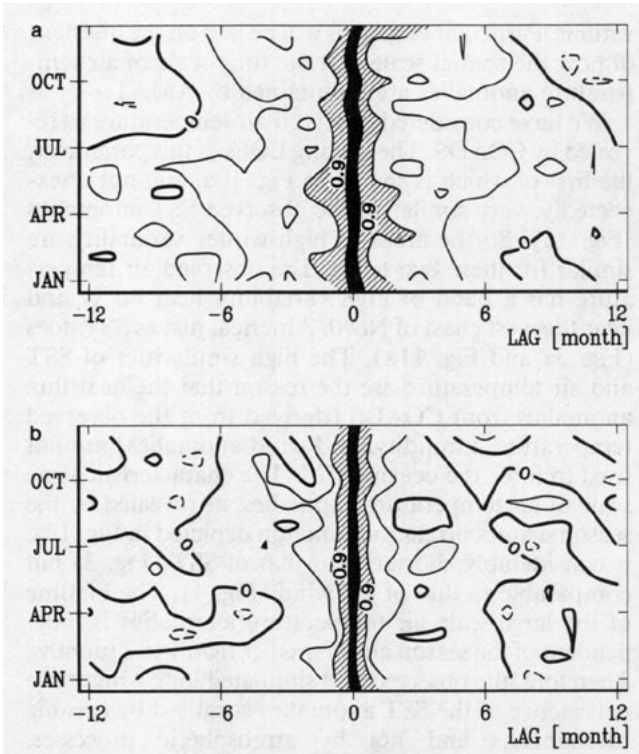


FIG. 12. Autocorrelation coefficients of the EOF time series (first EOF of the observed and simulated air temperature anomalies; see Fig. 11) for different seasons (January to December) and different lags (−12 to zero to 12 months). Black area: values greater than 0.9; hatched area: 0.6 to 0.9; dashed lines: negative values. (a) Observation (COADS). (b) Simulation (experiment A1: uncoupled).

served SSTs, are quite similar to the leading EOFs of the observed air temperature. The first simulated and observed EOFs are shown in Fig. 10. Not only the spatial scales but also the temporal scales of the air temperature are reproduced (Fig. 12). In the simulation the lifetime is slightly shorter than in the observations. A stronger SST forcing of AMAT as given in the model experiment can increase the lifetime. Interestingly, the first two EOFs of the simulated air temperature EOFs in experiment A1 have the same centers of action as the first two EOFs of simulated SST in the basic experiment. So the shift of the center of the coastal anomaly to the southwest as seen in the basic experiment is connected with AMAT.

In winter the similarity between observations and the A1 simulation is quite satisfactory: in January (Fig. 13a) the local correlation coefficient is higher than 0.5 in almost the entire analysis domain, and in large areas even higher than 0.75 (values greater than 0.54 are significantly nonzero, with a risk of less than 0.1%); maximum local correlations are in the western and the eastern part of the analysis domain, including areas with high observed air temperature variability (cf. Fig. 11). The wintertime air temperature variability is overestimated in the experiment (Fig. 11b). In summer, AMAT is much less skillful.

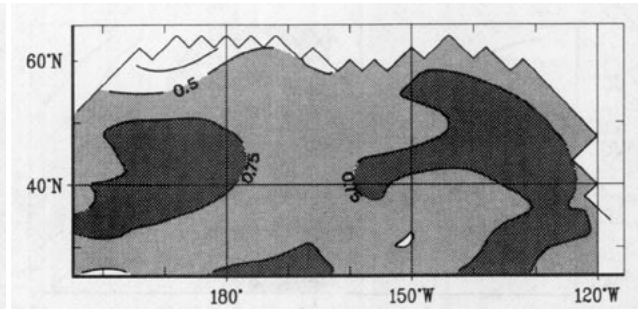


FIG. 13. Local correlation coefficients in January between observed (COADS) and simulated air temperature (experiment A1: uncoupled; 30 month; contour interval: 0.25). Areas with correlation coefficients greater than 0.50 (0.75) are stippled (dark stippled). Areas with negative values are hatched.

In experiment A2, the effect of the heat exchange with the ocean has been disregarded [$Q^*_{HS} = 0$ in (3)]. Instead, the air temperature is changed only by the diffusion and advection. Neglecting the turbulent sensible heat flux in AMAT has no significant effect on the spatial scales; instead, the leading EOFs of air temperature are almost unchanged from what they are in the basic experiment (not shown). This demonstrates that the horizontal scales of monthly mean air temperature anomalies are advectively forced by the anomalous monthly mean wind field, which is independent of the turbulent heat exchange with the ocean.

The largest difference, as compared to experiment

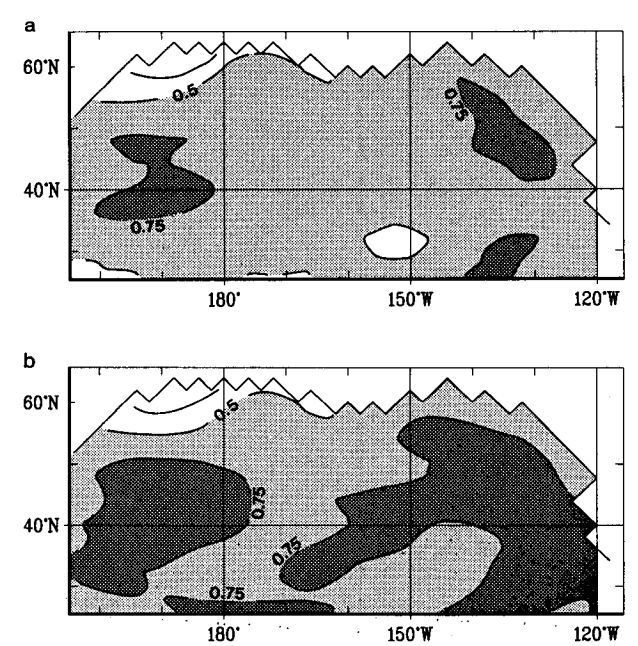


FIG. 14. Local correlation coefficients between observed (COADS) and simulated air temperature in January (30 month; contour interval: 0.25). Areas with correlation coefficients greater than 0.50 (0.75) are stippled (dark stippled). Areas with negative values are hatched. (a) Experiment A2: advective transports only; (b) experiment A3: uncoupled with $Q^*_{HL}$.

A1 or to the basic experiment, is in AMAT's skill in reproducing the observed air temperature anomalies. The local correlation coefficients in experiment A2 (Fig. 14a) are almost everywhere smaller than A1 (Fig. 13). Not unexpectedly, maximum reductions are in that part of the analysis domain where observed SST and air temperature are maximally correlated.

In experiment A3, in addition to $Q^*_{HS}$ a crude parameterization of the anomalous latent heat flux $Q^*_{HL}$ has been included. It is assumed that the water vapor is condensed at the same grid point where it is evaporated. For the parameterization of $Q^*_{HS}$ we used the bulk formulation (5), but multiplied by $-1$. This means that in AMAT condensation leads to a positive heat flux instead of a negative flux in the oceanic GCM. In this experiment the horizontal scale is again nearly unchanged in comparison with the results of the basic experiment. The heat exchange with the ocean leads to a slightly longer lifetime of the air temperature anomalies. The local correlations between simulated and observed air temperature anomalies become visibly stronger as the influence of the ocean increases (Fig. 14b).

## 6. "ENSO" experiment

An ENSO-related wind field is used to study the teleconnection via the atmosphere (see Introduction). The remote effect, excited by ENSO-related tropical atmospheric and oceanic anomalies, on the extratropical atmosphere is hypothesized to be instrumental in generating the ENSO-related North Pacific SST anomalies. In this section we investigate this hypothesis.

To do so, the ocean model and AMAT are forced by a wind field consisting of the climatological wind plus a synthetic wind anomaly ($\mathbf{u}^E = \mathbf{u}^C + \mathbf{u}^{E*}$), which is supposed to represent the ENSO-related wind forcing. These synthetic wind anomalies $\mathbf{u}^{E*}$ have been obtained by locally regressing the observed wind anomalies $\mathbf{u}^*$ with the Southern Oscillation index (SOI) by minimizing

$$\sum_t (\mathbf{u}^*(x, y, t) - \kappa_p(x, y, t) \cdot \mathrm{SOI}(t))^2. \quad (6)$$

Here $t$ is the time and the SOI is an area average of the SST anomalies in the eastern equatorial Pacific (6°N to 10°S; Wright et al. 1985). El Niño events are associated with positive SOI values. The bivariate vector of the regression coefficients $\kappa_p = (\kappa_x; \kappa_y)$ is found for each month $t_P$ (January to December) and for every grid point $(x, y)$. The components $\kappa_x$ and $\kappa_y$ represent the regression between the components of the wind vector $\mathbf{u}^* = (u_x; u_y)$ and the SOI.

With the regression model (6) the ENSO-related wind field is defined as

$$\mathbf{u}^{E*}(x, y, t) = \kappa_p(x, y, t) \cdot \mathrm{SOI}(t). \quad (7)$$

From autumn (September–October) to spring (April–May) the synthetic wind field has a westerly wind zone near 40°N and southerly winds near the North American coast if the SOI is positive; conversely, a negative SOI is connected to an anticyclonic pattern. In summer there is no such large-scale pattern.

To evaluate the statistical stability between (observed or simulated) SST and the observed SOI, we derive for each grid point and month the correlation coefficient $r$. A local correlation of $r$ indicates that the SOI is capable of explaining $r^2 \times 100$ percent of the variance of SST at that point and in that month. Thus, if $r = 0.25$, the SOI can explain 6% of the variance of the wind component, whereas if $r = 0.5$ or 0.75, the SOI explains 25% or 56%. Since we are estimating the correlation coefficients from samples of 30, $r = 0.24$ (0.31) is significantly nonzero at a level of 90% (95%).

In winter the SOI is positively correlated with SST near the North American coast and negatively correlated in the western and central North Pacific (Fig. 15a). The correlation pattern is large scale, but the absolute values are generally low: the January correlations are typically of the order of 0.3 to 0.5. The pattern of observed correlations is reproduced in the ENSO experiment (Fig. 15b) and, interestingly, also in the basic experiment (not shown). In the ENSO experiment the strength of correlation between SOI and simulated SST is considerably larger than in the observations, with maximum values of more than 0.75. In the basic experiment the correlations are comparable

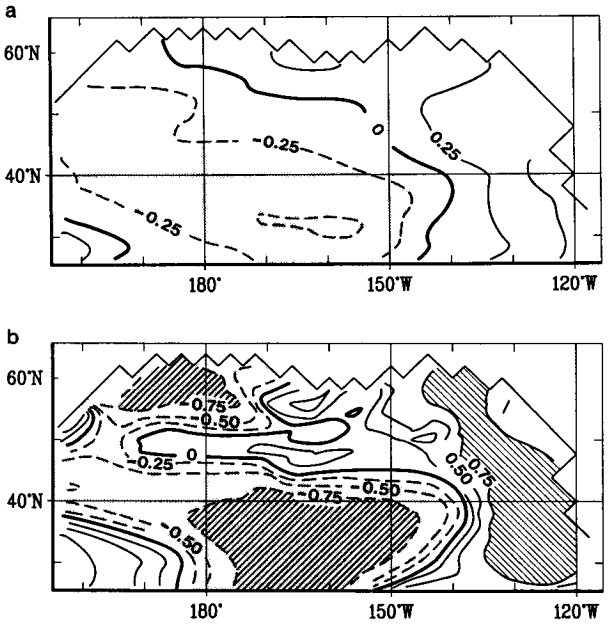


FIG. 15. Local correlation coefficients in January between SOI and SST (30 month; contour interval: 0.25). Areas with correlation coefficients less than −0.25 are stippled. Areas with correlation coefficient less than −0.75 or greater than 0.75 are hatched. (a) observed SST. (b) ENSO experiment.

to the observed ones. In the area of strong negative correlations about 10% to 30% of the wintertime variance can be explained by ENSO. Forced by an ENSO-related wind field, more than 50% of the SST variance can be explained by ENSO.

A significant correlation pattern between North Pacific SST and ENSO starts to evolve in September/October, with a strength and distribution similar to that in January (Fig. 15). In summer, the correlation coefficients obtained for observed and simulated SST are much weaker.

The results of the ENSO experiment support the concept that the observed link between ENSO and the North Pacific SST is maintained by atmospheric teleconnections. However, the SOI is not a powerful nowcaster of North Pacific SST; it accounts for only 10% to 30% of the SST wintertime variance—in the observed data as well as in the basic experiment. This is so because large-scale atmospheric circulation anomalies in the North Pacific area are affected not only by the ENSO-related teleconnections but even more by the macroturbulent processes of extratropical atmospheric flow.

## 7. Conclusions

### *a. The overall performance of the coupled OGCM/AMAT model*

The coupled atmosphere–ocean model, consisting of a regular ocean GCM and the highly simplified advective model of the air temperature (AMAT), each driven by observed winds, is able to reproduce the observed large-scale (about 2500 to 6000 km) patterns of the North Pacific SST as a response to large-scale atmospheric circulation anomalies. The time characteristics of observed SST, namely, a high persistence of anomalies in winter of up to 4 to 6 months and lower persistence in summer, are well matched by the model simulation. Moreover, in winter, the time coefficients of the spatial patterns resemble the observations very well. Also, the local wintertime correlations are high, particularly in the region of high SST variability near 40°N. In summer the similarities between observation and simulation are much smaller.

We find that the specification of anomalous turbulent heat fluxes is essential for a good representation of the SST by the ocean model. In the present study these fluxes are parameterized in a rather crude manner by using standard bulk-transfer formulas and the AMAT. The role of advective processes in the ocean for the formation of SST anomalies turns out to be of second-order importance, and the diffusivity processes are of third order.

### *b. Scales*

Interestingly, the characteristic large-scale patterns of the air temperature are directly related to the large-scale atmospheric circulation anomalies. At the same time, the large-scale patterns of SST and air temperature are very similar. That means that the horizontal scale is transferred nearly unchanged from the atmosphere to the ocean; it is hardly affected by oceanic processes.

In the time domain, however, the air temperature anomalies and the SST anomalies behave differently in a characteristic way. First, the oceanic anomalies lag the atmospheric ones by about one month. Second, the characteristic time scale, which is of the order of two weeks for the atmospheric parameters, is considerably longer for the SST. This is particularly pronounced in winter, when the mixed layer is deep. The ocean response integrates over the higher atmospheric fluctuations.

### *c. Limitations of the experiments*

In the coupled OGCM/AMAT model a number of processes have not been taken into account.

In the ocean model the mixed-layer dynamics has not been parameterized explicitly. Instead, the mixed layer was modeled by parameterization of turbulent vertical mixing and convective adjustment in the upper levels of the OGCM. The observed deep-winter mixed layer (about 100 to 200 m; Bathen 1972; Levitus 1982) and seasonal variations are mainly reproduced by the model. But in summer the vertical resolution (first layer 20 m thick) is too coarse for a good representation of the observed shallow mixed layer (about 20–50 m; Levitus 1982). Another simplification in the OGCM is in its salinity budget. Because of the lack of observed precipitation data over the ocean, the dependence of the upper-ocean density structure on anomalous forcing has not been considered.

The most efficient processes in the ocean's surface heat balance are probably anomalies of the turbulent latent and sensible heat fluxes and of the radiative forcing. The latter has not been taken into account. Our results seem to indicate that anomalous radiation, due to clouds, is not significant in winter; in summer, however, this process might be much more important for the development of the SST anomalies in the North Pacific due to the stronger summer solar insolation.

To force both the OGCM and AMAT monthly mean wind fields have been used, disregarding the effect of high-frequency events in the wind field, such as storms. Strong storms potentially have a strong impact on the mixed layer and, thus, on the lifetime of SST anomalies. In spring these atmospheric fluctuations smaller than one month might be important. The success of our simulations in winter shows that this effect is not of first order.

We conclude that, in spite of the relatively coarse horizontal and vertical resolution of the models and in spite of the imposed simplifications, our coupled

OGCM/AMAT model is quite capable of reproducing the space–time statistics of SST, particularly in winter.

### d. *ENSO teleconnections*

Our experiments suggested that the ENSO-related part of the North Pacific SST anomalies can be explained as the local oceanic response to midlatitude wind anomalies excited by tropical ENSO anomalies. In the case of directly ENSO-related atmospheric circulation more than 50% of the SST variance can be explained by ENSO. However, in the observed wind field this ENSO-related signal is fairly weak, even though it is statistically stable: the skill of the Southern Oscillation index (SOI) in specifying the North Pacific SST is, in winter, only of the order of 10%–30%.

*Acknowledgments.* The OGCM has been developed by Dr. Ernst Maier-Reimer. Drs. Nanne Weber, Richard Kleeman, Arie Kattenberg, Peter Wright, and Grant Branstator helped us with valuable comments. Compilation of COADS data at the MPI was accomplished by Peter Wright. The diagrams were thoroughly prepared by Marion Grunert and Doris Lewandowski. We wish to thank all of them. The work was part financed by the European Community Climate Program under Grant EV4C-0035-D(B).

## REFERENCES

Alexander, M. A., 1990: Interaction between the North Pacific Ocean and the Northern Hemisphere during El Niño. Ph.D. thesis, University of Wisconsin—Madison, Madison, WI, 150 pp.

Barnston, A. G., and R. E. Livezey, 1987: Classification, seasonality and persistence of low-frequency atmospheric circulation patterns. *Mon. Wea. Rev.*, **115**, 1083–1126.

Bathen, K. H., 1972: On the seasonal changes in the depth of the mixed layer in the North Pacific Ocean. *J. Geophys. Res.*, **77**, 7138–7150.

Bjerknes, J., 1962: Synoptic survey of the interaction between sea and atmosphere in the North Atlantic. *Geofys. Publ.*, **24**, 116–145.

——, 1964: Atlantic air–sea interaction. *Adv. Geophys.*, **10**, 1–82.

——, 1969: Atmospheric teleconnections from the equatorial Pacific. *Mon. Wea. Rev.*, **97**, 163–172.

——, 1972: Large-scale atmospheric response to the 1964–65 Pacific equatorial warming. *J. Phys. Oceanogr.*, **2**, 212–217.

Cayan, D. R., 1990: Variability of latent and sensible heat flux over the oceans. Ph.D. thesis, University of California, San Diego, CA, 199 pp.

Chervin, R. M., J. E. Kutzbach, D. D. Houghton, and R. G. Gallimore, 1980: Response of the NCAR general circulation model to prescribed changes in ocean surface temperature: II. Midlatitude and subtropical changes. *J. Atmos. Sci.*, **37**, 308–332.

Davis, R. E., 1976: Predictability of sea surface temperature and sea level pressure anomalies over the North Pacific Ocean. *J. Phys. Oceanogr.*, **6**, 249–266.

Frankignoul, C., 1985: Sea surface temperature anomalies, planetary waves, and air–sea feedback in the middle latitudes. *Rev. Geophys.*, **23**, 357–390.

——, and K. Hasselmann, 1977: Stochastic climate models. II: Application to sea-surface temperature variability and thermocline variability. *Tellus*, **29**, 284–305.

——, and R. W. Reynolds, 1983: Testing a dynamical model of midlatitude sea surface temperature anomalies. *J. Phys. Oceanogr.*, **13**, 1131–1145.

Hamilton, K., 1988: A detailed examination of the extratropical response to the tropical El Nino/Southern Oscillation events. *J. Climatol.*, **8**, 67–86.

Haney, R. L., 1980: A numerical case study of the development of large-scale anomalies in the central North Pacific Ocean. *J. Phys. Oceanogr.*, **10**, 541–556.

——, 1985: Midlatitude sea surface temperature anomalies: A numerical hindcast. *J. Phys. Oceanogr.*, **15**, 787–799.

——, W. S. Shiver, and K. H. Hunt, 1978: A dynamical-numerical study of the formation and evolution of large-scale ocean anomalies. *J. Phys. Oceanogr.*, **8**, 952–969.

Hasse, L., and F. Dobsen, 1986: *Introductory Physics of Atmosphere and Ocean.* D. Reidel, 126 pp.

Hasselmann, K., 1976: Stochastic climate models. Part I: Theory. *Tellus*, **28**, 473–485.

Hellerman, S., and M. Rosenstein, 1983: Normal monthly wind stress over the world ocean with error estimates. *J. Phys. Oceanogr.*, **13**, 1093–1104.

Herterich, K., and K. Hasselmann, 1987: Extraction of mixed layer advection velocities, diffusion coefficients, feedback factors and atmospheric forcing parameters from the statistical analysis of the North Pacific SST anomaly fields. *J. Phys. Oceanogr.*, **17**, 2146–2155.

Horel, J. D., and J. M. Wallace, 1981: Planetary-scale atmospheric phenomena with the Southern Oscillation. *Mon. Wea. Rev.*, **109**, 813–829.

Huang, J. C. K., 1979: Numerical case studies for oceanic thermal anomalies with a dynamical model. *J. Geophys. Res.*, **84**, 5717–5726.

Jacob, W. J., 1967: Numerical semiprediction of monthly mean sea surface temperature. *J. Geophys. Res.*, **72**, 1681–1689.

Lau, N.-C., and M. J. Nath, 1990: A general circulation model study of the atmospheric response to extratropical SST anomalies observed in 1950–79. *J. Climate*, **3**, 965–989.

Levitus, S., 1982: Climatological atlas of the world ocean. NOAA Professional Paper 13. U.S. Govt. Printing Office, Washington, D.C., 173 pp.

Livezey, R. E., and K. C. Mo, 1987: Tropical-extratropical teleconnections during Northern Hemisphere winter. Part II: Relationships between monthly mean Northern Hemisphere circulation patterns and proxies for tropical convection. *Mon. Wea. Rev.*, **115**, 3115–3132.

Luksch, U., H. V. Storch, and E. Maier-Reimer, 1990: Modeling North Pacific SST anomalies as a response to anomalous atmospheric forcing. *J. Mar. Sys.*, **1**, 155–168.

Mo, K. C., and R. E. Livezey, 1986: Tropical–extratropical geopotential height teleconnections during the Northern Hemisphere winter. *Mon. Wea. Rev.*, **114**, 2488–2515.

Namias, J., 1959: Recent seasonal interactions between North Pacific waters and the overlying atmospheric circulation. *J. Geophys. Res.*, **64**, 631–646.

——, 1965: Macroscopic association between mean monthly sea surface temperature and the overlying winds. *J. Geophys. Res.*, **70**, 2307–2318.

——, 1969: Seasonal interactions between the North Pacific Ocean and the atmosphere during the 1960's. *Mon. Wea. Rev.*, **97**, 173–192.

——, and D. R. Cayan, 1981: Large-scale air–sea interaction and short-period climate fluctuations. *Science*, **214**, 869–876.

——, X. Yuan, and D. R. Cayan, 1988: Persistence of North Pacific sea surface temperature and atmospheric flow patterns. *J. Climate*, **1**, 682–703.

Pacanowski, R. C., and S. G. H. Philander, 1981: Parameterization of vertical mixing in numerical models of tropical oceans. *J. Phys. Oceanogr.*, **11**, 1443–1451.

Reynolds, R. W., 1978: Sea-surface temperature in the North Pacific Ocean. *Tellus,* **30,** 97–103.

UNESCO, 1981: Tenth report of the joint panel on oceanographic tables and standards. UNESCO Technical Papers in Marine Sci., No. 36, UNESCO, Paris.

Wallace, J. M., and D. S. Gutzler, 1981: Teleconnections in the geopotential height field during the northern Hemisphere winter. *Mon. Wea. Rev.,* **109,** 784–812.

——, and Q. Jiang, 1987: On the observed structure of the interannual variability of the atmosphere/ocean system. *Atmospheric and Oceanic Variability,* H. Cattle Ed., Roy. Meteor. Soc., Bracknell, 17–43.

——, C. Smith, and Q. Jiang, 1990: Spatial patterns of atmosphere/ocean interaction in the northern winter. *J. Climate,* **3,** 990–998.

Weare, B. C., A. R. Navato, and R. E. Newell, 1976: Empirical orthogonal analysis of Pacific sea surface temperatures. *J. Phys. Oceanogr.,* **6,** 671–678.

White, W. B., G. A. Meyers, J. R. Donguy, and S. E. Pazan, 1985: Short-term variability in the thermal structure of the Pacific Ocean during 1979–1982. *J. Phys. Oceanogr.,* **15,** 917–935.

Woodruff, S. D., R. J. Slutz, R. L. Jenne, and P. M. Steurer, 1987: A comprehensive ocean–atmosphere data set. *Bull. Amer. Meteor. Soc.,* **68,** 1239–1250.

Wright, P. B., 1983: Sea surface temperature fluctuations in the Pacific, 0-50N. *Trop. Ocean–Atmos. Newslett.,* **19,** 14–15.

——, T. P. Mitchell, and J. M. Wallace, 1985: Relationships between surface observations over the global oceans and the Southern Oscillation. Pacific Marine Environ. Lab., Seattle, ERL/NDAA Data Report, PMEL-12.

Zorita, E., V. Kharin, and H. v. Storch, 1992: The atmospheric circulation and sea surface temperature in the North Atlantic area in winter: Their interaction and relevance for Iberian precipitation. *J. Climate,* submitted.